available at www.sciencedirect.com

ScienceDirect

journal homepage: www.elsevier.com/locate/carbon

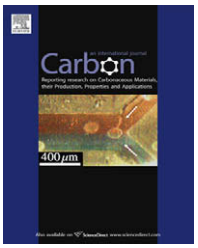

Characterization of graphite implanted with chlorine ions using combined Raman microspectrometry and transmission electron microscopy on thin sections prepared by focused ion beam

M.R. Ammar [a,*], J.N. Rouzaud [a], C.E. Vaudey [b], N. Toulhoat [b,c], N. Moncoffre [b]

[a] Laboratoire de Géologie de l'Ecole Normale Supérieure, UMR CNRS-ENS 8538, 24 rue Lhomond, F-75231 Paris cedex 5, France
[b] Université Lyon 1, CNRS/IN2P3, UMR5828, Institut de Physique Nucléaire de Lyon (IPNL), 4 rue Enrico Fermi, F-69622 Villeurbanne cedex, France
[c] Commissariat à l'Energie Atomique CEA/DEN, Centre de Saclay, F-91191 Gif sur Yvette cedex, France

ARTICLE INFO

Article history:
Received 18 September 2009
Accepted 27 November 2009
Available online 2 December 2009

ABSTRACT

Graphite was modified by 250 keV $^{37}Cl^+$ ion implantation. Combined Raman microspectrometry/transmission electron microscopy (TEM) studies have been used to characterize the multiscale organization of the graphite structure. The penetration depth of $^{37}Cl^+$ into the graphite sample was limited to the surface (~200 nm) because of the dissipation of the irradiating ion energy as expected by secondary ion mass spectrometry analysis. Raman microspectrometry appears to be an appropriate tool for studying such scales. Spectra showed a strong increase of defect bands after implantation at a fluence of $5 \cdot 10^{13}$ ions/cm^2. In order to examine the structural degradation of the graphite versus the depth at the nanometer scale, the focused ion beam technique seems to be a well-suited method for a relevant coupling of Raman and TEM observations.

1. Introduction

Ion beam irradiation (or implantation) has been used to modify the physical and chemical properties of materials [1–6]. It has frequently been used to reduce corrosion [7], improve wear resistance of materials [8], and to reduce the formation of oxidation layers on the metal surface [9]. Such implantation introduces a wide range of defects in a controlled manner whatever the nature of the incident irradiation because the latter plays a minor role [10]. However, the penetration depth into the bulk materials, even through a high energy ion irradiation, is limited to the surface because of the rapid dissipation of the irradiating ion energy [11,12].

The application of Raman microspectrometry for the characterization, at a micrometer scale, of the graphite structure after ion implantation (ion-implanted graphite), is well suited since the penetration depth of a Raman laser into graphite is 80–100 nm [13,14]. Indeed, several authors have studied the structural modifications of graphite using this technique because it has a high spatial resolution (~1 μm) and provides less averaged information, in comparison with X-ray diffraction (XRD) [15–18]. Moreover, analyses are rapid, operationally straightforward, non-destructive and require minimal sample preparation, characteristics that make Raman microspectrometry particularly attractive.

Transmission electron microscopy (TEM) allows for its part the direct imaging of the polyaromatic layers profile and consequently the access to the multiscale organization in the nanometer–micrometer range. However, the quantification of the structural order or disorder is not easy, whereas Raman

* *Corresponding author:* Fax: +33 01 44 32 20 00.
E-mail address: ammar@geologie.ens.fr (M.R. Ammar).
0008-6223/$ - see front matter
doi:10.1016/j.carbon.2009.11.049

is a 'blind' method but gives nevertheless quantitative information on the structural defects. Therefore, Raman microspectrometry and TEM appear to be complementary techniques and their cross-utilization was chosen here to obtain a pertinent structural characterization of ion-implanted graphite.

In fact, numerous TEM studies on the structure of different carbons have already been reported [19–22]. However, the observation by TEM of the nanostructural changes caused by the ion beam irradiation at the surface, or near the surface, cannot easily be achievable by conventional techniques such as hand grinding, ultramicrotomy and mechanical abrasion or ion thinning. Moreover, all these methods have additional disadvantages. For instance, ion thinning could cause noticeable graphite amorphization. Ultramicrotomy is extremely complicated to perform due to difficulty to precisely select, at the micrometer scale, a region of interest from which to produce the thin sections [23]. In the case of our graphite, the modified zone forms a micrometer thick skin at the surface of centimeter sized platelets. The production of thin sections perpendicular to the platelet does not appear to be trivial; this necessitates cutting a millimeter thick slice of platelet, putting it flat into a mould and to embed it in resin in an orientation allowing at first the cut of the modified zone by a diamond knife. Moreover, decohesions and possible tearing could preferentially occur between 'structurally modified' and virgin graphite, i.e., when differences in hardness occur. Similar problems could be also considered as far as mechanical abrasion is concerned.

The process which can provide a great advance in the study of the ion-implanted graphite is the use of thin sections prepared by the focused ion beam (FIB) technique. In fact, the very important benefit of this method is the easy and direct control of the choice of the area, the sample orientation according to the beam and the specimen thickness during ion milling [23]. This state-of-the-art preparation method of thin sections (<100 nm) for TEM observation has been used intensively in various fields such as geosciences [24–32] and has been demonstrated in many applications. It was first used in scanning ion microscopy [33] and lithography [34], gas-assisted etching and deposition [35], failure analysis [36] and modification of integrated circuits and multicomponent devices [37].

In the present study, we have applied the FIB technique which offers a great opportunity to combine Raman and TEM studies of ion-implanted graphite. We reported studies on the graphite implanted with 250 keV ^{37}Cl, at a fluence of $5 \cdot 10^{13}$ ions/cm^2. The profile depth of ^{37}Cl has been followed by secondary ion mass spectrometry (SIMS) which is widely used due to its high sensitivity and its ability to reproduce the in-depth profiles of elements [38–40].

2. Experimental

2.1. Sample preparation

The sample of virgin graphite is a nuclear graphite (highly graphitized petroleum coke–pitch carbon–carbon composite) used as a moderator in the "uranium natural graphite gas" (UNGG) nuclear reactors. It was implanted at room temperature using the 400 kV ion implanter of the Institute of Nuclear Physics of Lyon (IPNL, Lyon, France). The sample was implanted with a 250 keV $^{37}Cl^+$ ion beam at a fluence of $5 \cdot 10^{13}$ ions/cm^2.

The FIB method was used to prepare thin sections of the ion-implanted graphite. It was performed with an FEI STRATA DB 235 FIB dual beam system at the institut d'électronique de microélectronique et de nanotechnologie (IEMN, Lille, France). The system combines scanning electron beam and ion beam modes as two units of a single instrument. This method is described in more detail in [41,42]. The FIB system uses a Gallium liquid metal as ion source. A thin layer of platinum was first deposited in order to protect the specimen surface during the milling process. In order to avoid any potential damage to the sample surface during electron beam deposition of the Pt strap, samples were previously coated with a thin (~30 nm) layer of palladium–gold (Pd–Au) using a sputter coater (Polaron SC 7620) before being inserted into the FIB chamber. A 30 kV Ga^+ beam operating at ~20 nA excavated the sample from both sides of the Pt layer to a depth of about 5 μm. By using a micromanipulator, the sample is removed and transferred to a TEM grid. The last step involves the final thinning of the sample, resulting in a section at about 15 μm × 5 μm, with a thickness of about 100 nm, thus making it electrons transparent. For images of the various stages of milling process, see [25,26,30].

2.2. Characterization

2.2.1. Raman microspectrometry

Raman microspectrometry was used to evaluate the structural change resulting from the chlorine implantation. Studies were performed in ambient conditions by using a Renishaw INVIA spectrometer equipped with an Ar laser source, focused through a Leica microscope. The Rayleigh scattering component was removed by a Notch filter, and the Raman-scattered light was dispersed by a holographic grating with 1800 lines/mm and detected by a CCD camera. The spectra were collected under microscope (x50 objective) using the 514.5 nm wavelength (2.41 eV). Very low incident power (1–5 mW) was used to avoid heating effects [21,22,42,43]. Each spectrum represents the average of three measurements (Fig. 1).

2.2.2. Transmission electron microscopy

Thin sections prepared by the FIB technique were investigated using TEM JEOL 2011 microscope operating at 200 kV. The graphite nanostructure can be directly imaged coupling various TEM modes [20,44]. In the present study, we used mainly the dark field (11DF) mode and the 002 lattice fringe mode (often called "high-resolution" mode). 11 dark field mode is an amplitude contrast technique, enabling the imaging of "moiré" fringes formed by superimposed crystallites lying flat. The extent of homogeneous moiré fringes area, both in direction and in period, permits to measure L_a the diameter of the coherent domain or the Basic Structural Units (BSU). By using the 002 lattice fringe technique (002LF), it is possible to directly image the profile of the polyaromatic layers.

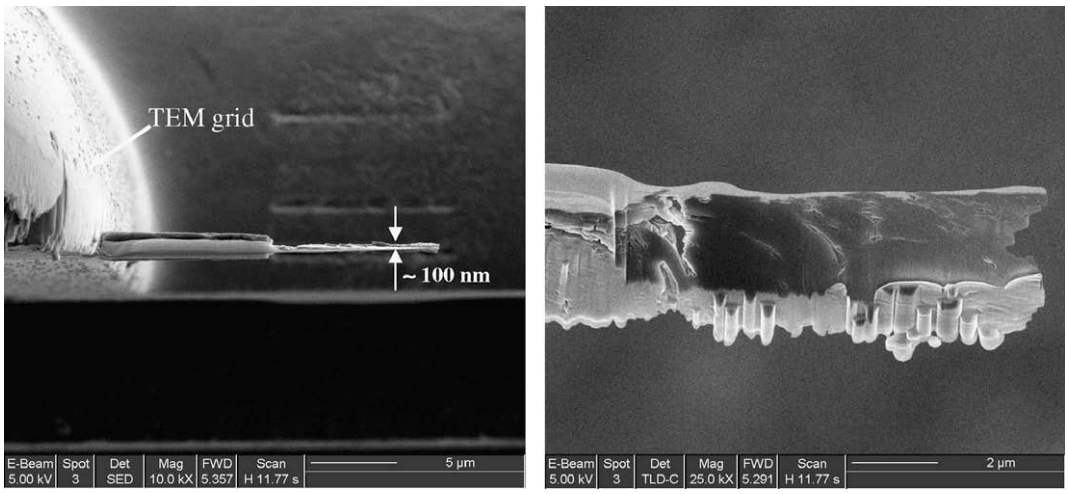

Fig. 1 – Secondary electron microscopy images recorded after FIB thining, showing two orthogonal views of a completely thinned sample.

2.2.3. Secondary ion mass spectrometry

The ^{37}Cl depth profiles were analyzed with a CAMECA IMS 6f SIMS facility at the "Ecole des Mines de Paris" at Fontainebleau, France. The focused primary beam was scanned over an area of 150 × 150 μm^2 on the sample surface. Secondary ions were collected from a smaller region (8 μm in size) located in the center of the sputtered area in order to minimize crater-edge effects. The analysis was made with a Cs^+ primary ion beam of about 8 nA intensity. Negative secondary $^{37}Cl^-$ ions (mainly implanted ions), and $^{12}C^-$ ions (matrix ions) were collected. As the $^{12}C^-$ signal does not vary, it was used as a reference to normalize the $^{37}Cl^-$ signal. The depth scale for each sputtered profile was determined by measuring the crater depth by optical interferometry at the Institut National des Sciences Appliquées (INSA, Lyon, France), using a FOGAL device [45]. The depth resolution was estimated to be around 50 nm at the bottom of the crater. The uncertainty of the measurement can be explained by two means: the remaining sample surface roughness (0.2 μm) and the differential erosion rates due to local graphite heterogeneities (more or less graphitized zones due to different carbon compounds) [46]. $^{37}Cl^-$ intensities were converted to ^{37}Cl atomic concentrations, by normalizing the area of the implanted SIMS profile by the area of the profile calculated with the stopping and range of ions in matter (SRIM) software (based on Monte Carlo calculations) [47].

3. Result and discussion

Fig. 2 shows Raman spectra of the single crystalline graphite (highly oriented pyrolytic graphite (HOPG)) and the nuclear graphite. They are divided into first and second-order regions. The first order Raman spectrum of single crystalline graphite (HOPG) (Fig. 2a), normally consists of two vibrational modes E_{2g} with D^4_{6h} symmetry, i.e. to in-plane bond stretching of aromatic carbons in the graphitic structure, situated at 42 (not shown here) and 1581 cm^{-1} respectively [48]. The most studied is the so-called G "Graphite" band at around 1581 cm^{-1}

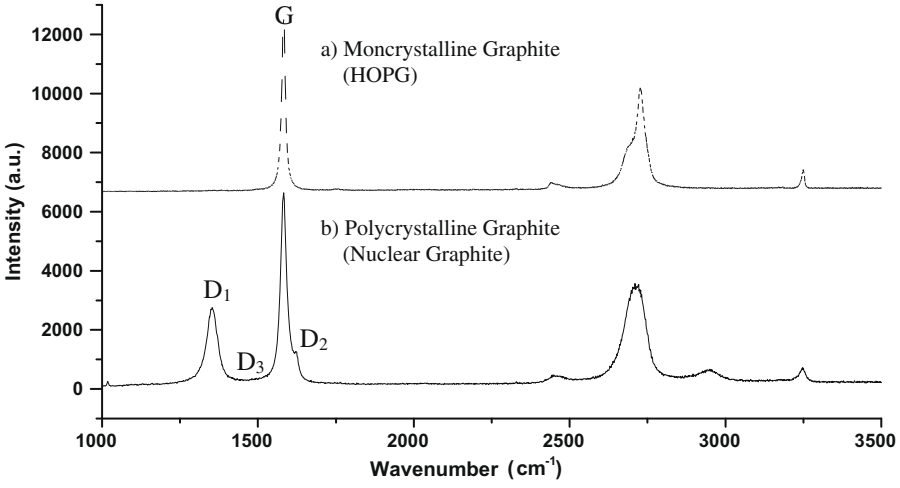

Fig. 2 – Raman spectra obtained with λ_0 = 514.5 nm showing the first and second-order regions of (a) high oriented pyrolitic graphite (HOPG) (dotted line) and (b) virgin graphite.

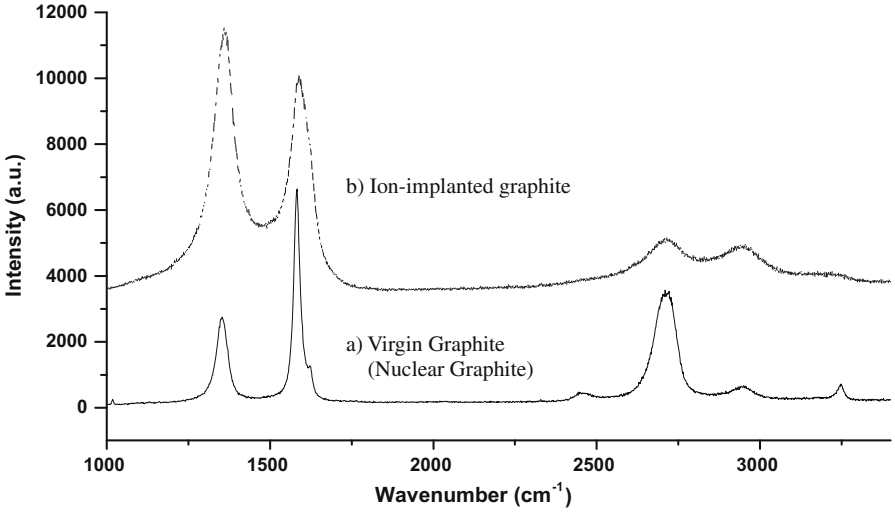

Fig. 3 – Raman spectra, obtained with λ_0 = 514.5 nm, of (a) virgin graphite and (b) graphite implanted (dotted line) with ^{37}Cl at a fluence of $5 \cdot 10^{13}$ ions/cm^2 and at room temperature.

[48,49]. The nuclear graphite is a polycrystalline carbon consisting of large numbers of finite sub-micrometer-sized graphitic crystallites. Raman spectrum of such polycrystalline graphite exhibits additional bands called D for "Defect" bands (Fig. 2b). They are known to be characteristic of imperfect crystalline graphite and to grow in intensity relative to the G band with increasing degree of disorder in the graphitic structure [19,49]. The band occurring at 1360 cm^{-1} (D_1 band) is usually the most intense defect band and was first attributed to breathing mode with A_{1g} symmetry. As proposed by Tuinstra and Koenig for a series of graphitic materials, the ratio I_{D1}/I_G is inversely proportional to the mean size (L_a) of the crystallites calculated by X-ray diffraction [49]:

$$R_1 = I_{D1}/I_G \propto 1/L_a$$

The 1620 cm^{-1} band (D_2 band) appears as a shoulder on the G band, and was assigned to a lattice vibration involving the distribution of graphene layers spacing at the surface [50]. The 1500 cm^{-1} band (D_3 band) is present in poorly ordered carbons as a very wide band. Beny-Bassez and Rouzaud attributed this band to the out-plane defects such as tetrahedral carbons (sp^3 carbons within sp^2 structures) [51].

Raman spectrum of a single crystal exhibits also the second order bands at about 2450, 2720, and 3240 cm^{-1} (Fig. 2a) attributed to overtones or combinations scattering [50]. The most intense, near 2700 cm^{-1}, splits into two bands and was then described as a characteristic feature of a perfect tri-periodic order met in undisturbed or a highly ordered graphite lattice [14].

The virgin nuclear graphite exhibits no pronounced split but has a relatively broad band; this indicates that the tri-periodic order is not perfect, as it is usual in these synthetic graphites obtained by heat-treatment at atmospheric pressure. An additional band is observed at 2950 cm^{-1} which has been assigned to a combination of the G and D modes characteristic of disturbed graphitic structures, (G + D) [52].

Fig. 3 shows Raman spectra (λ_0 = 514.5 nm) of virgin graphite and chlorine ion-implanted graphite. After implantation, we clearly observe a significant increase of the D_1 (~1350 cm^{-1}) and D_2 (~1585 cm^{-1}) band intensities relative to the G band, suggesting the occurrence of a highly disordered graphite in the modified zone. Such spectral modifications correspond to the decrease of the crystallites size since the Tuinstra and Koenig ratio R_1 varied from 0.4 for virgin graphite to 1.1 for ion-implanted graphite. We also observe an increase of the D_3 (~1500 cm^{-1}) band probably related to an increasing amount of sp^3 hybridized carbon atoms, responsible for a more and more amorphous character of the modified zone of ion-implanted graphite.

Secondary ion mass spectrometry (SIMS) was used here to characterize the penetration depth of chlorine after the ion implantation which is directly responsible for the defect formation. Fig. 4 displays the comparison between the SRIM calculated profile and the implanted experimental ^{37}Cl profile. The ^{37}Cl projected range (Rp) calculated with SRIM is 200 nm and the maximum of the ^{37}Cl concentration is around 50 ppm at. A spreading of the experimental profile over depth compared to the SRIM profile is observed. Vaudey et al. attributed this spreading to the porous texture of the nuclear

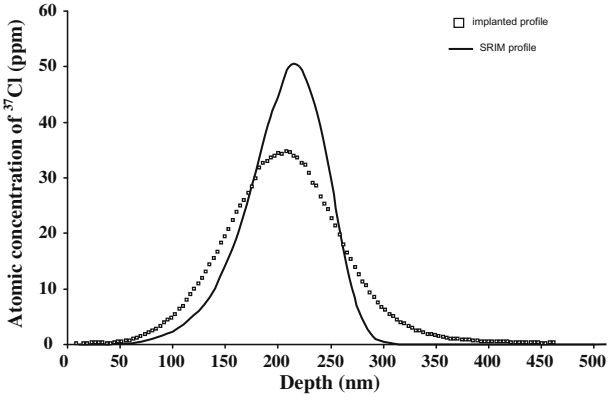

Fig. 4 – Comparison of the measured implantation profile with the profile calculated with the computer code SRIM 2008.

graphite (carbon–carbon composite) [46]. The presence of chlorine at this depth from the surface proves that the structural defect is also limited to the surface and that it is very complicated or even impossible from a technical aspect to observe this defect at a nanometer scale.

The results indicate that the FIB–SEM offers exceptional precision and seems to be an appropriate method for preparing thin sections for TEM examination of ion-implanted graphite (Fig. 5). The technique provides analytical access to very small scale features that are lost if the sample is prepared by conventional methods. In the studied thin section prepared by FIB (see Fig. 5a), the surface of the ion-implanted graphite appears on the top of the section, just below the protection layer (single arrow). The 002 lattice fringe mode was particularly used to image the profile of the aromatic layers in very small areas (30 nm × 30 nm). This allows to follow carefully, step by step, the organization from the near surface (ion-implanted graphite, Fig. 5c) up to the virgin graphite (Fig. 5e), through a zone less affected by ion implantation (Fig. 5d).

The results showed a dramatic change of the polyaromatic layers organization at the near surface according to 002 fringes (Fig. 5c), where the density of ^{37}Cl implantation was maximal. This explained the high increase of the defects

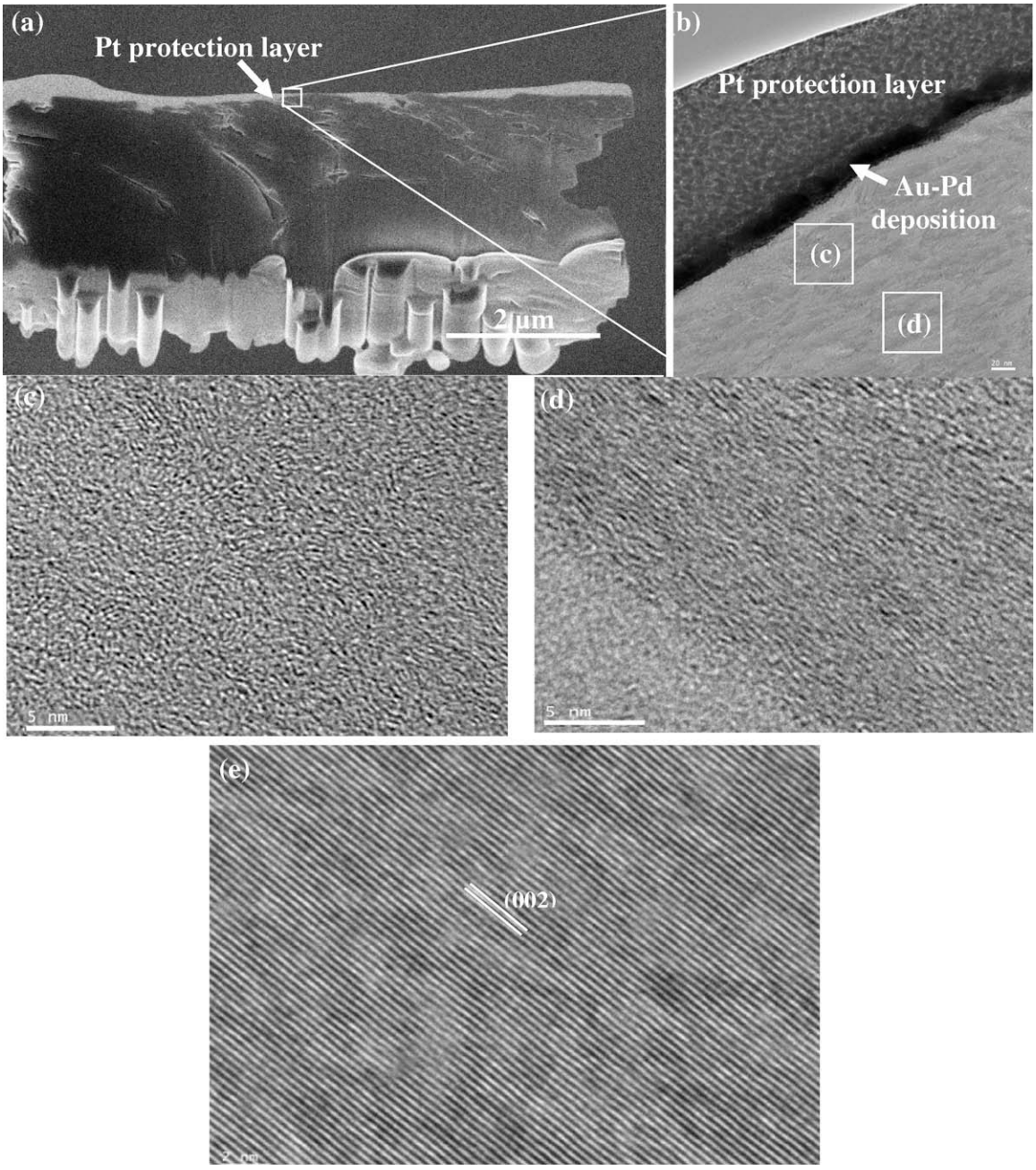

Fig. 5 – (a) Secondary electron image of the thin section prepared by the FIB of graphite implanted with chlorine at a fluence of 5×10^{13} ions/cm^2; (b) transmission electron microscopy image of the ion-implanted graphite that was coated with ~30 nm of Au-Pd prior to FIB work. (c)–(e) HRTEM images showing the evolution of 002 lattice fringes (002 LF) after ^{37}Cl implantation.

bands relative to the G band in Raman spectrum. However, the graphite structure was strongly damaged without becoming completely amorphous: only short nanometer-sized fringes forming small BSU (stacks of 2–3 layers) are visible and these stacks are strongly disoriented, losing the lamellar nanostructure of the virgin graphite. This is most probably due to the occurrence of sp^3 carbons having an angle of 109° with others sp^2 carbons, hence, the increase of the BSU disorientation. Geometrically speaking, such cross-linked BSU form nanopores. From the surface which was strongly affected by implantation up to virgin graphite where there is no implantation, the 002 lattice fringe mode showed more or less distorted polyaromatic layers (Fig. 5d), and eventually stiff, flawless, large (>>0.1 μm) and planar layers without any defects, corresponding to non-implanted zones (Fig. 5e).

The decrease of L_a, the coherent domain (BSU) diameter was confirmed by the measurement of the rotation moiré fringes in the 11DF dark field images. This phenomenon is due to the fact that two slightly rotated crystals give birth to two 11 beams close enough to each other to interfere, thus some moirés fringes appear [20,44] whereas, the crystals which do not fulfil the 110 Bragg condition remain dark (Fig. 6). In this study, the size of the largest coherent domains is about 200–300 nm for pristine graphite, and decreases to 50–100 nm for the most modified zone of graphite (Fig. 6).

The results obtained by TEM are in good agreement with those of Raman microspectrometry, and both methods are complementary. For a fluence of $5 \cdot 10^{13}$ ions/cm^2, a very disordered nanoporous carbon is obtained in the most implanted zone. However, a true amorphous carbon is not reached, since nanometer-length fringes remain visible, and Raman spectra still contain two well identified D and G bands.

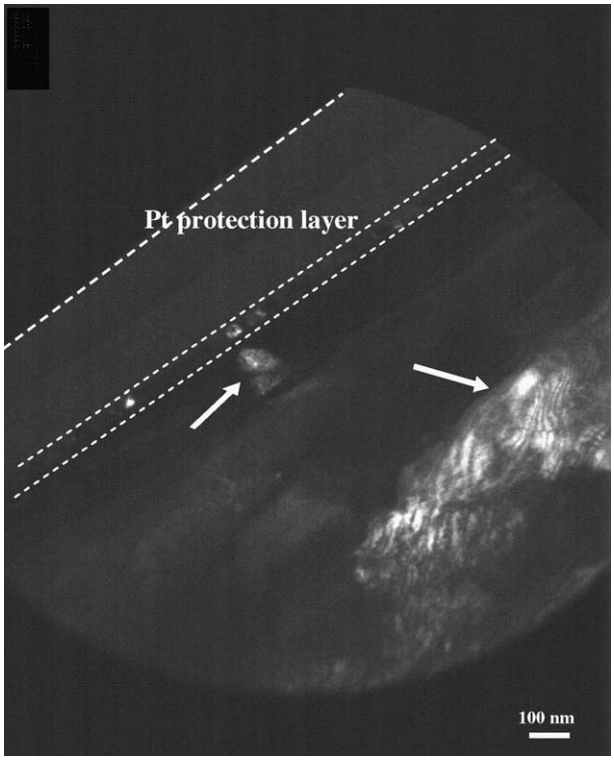

Fig. 6 – 11 Dark field micrograph of ion-implanted graphite showing a decrease of crystallites size near the surface, where the implantation was maximal.

Work is still in progress on the ion-implanted graphite at varying doses and implantation temperatures in order to emulate the effect of neutrons in the nuclear reactor and understand the basic physical radiation damage processes, for which neutron irradiation is often less well-suited. One of the major differences in the characteristics of ions and neutrons is their depth of penetration (over many millimeters of the materials for neutrons) [12]. Thus, the FIB-thinning technique appears to be an appropriate method for a relevant characterization of ion-implanted graphite since it allows an effective coupling of Raman and TEM.

However, it must be noted that the FIB should be used very carefully as the sample preparation technique may produce some artifacts like local Gallium implantation in the top surface of graphite, and also, depending on the material, the creation of a several nanometers-thick amorphous layer covering the sidewall of the graphite TEM specimen [26,53,54]. Such artefacts, which may impact TEM observations, can be largely avoided by following some precautions. The sample top surface can be successfully protected by depositing a platinum strap on the sample area of interest prior to the milling stage. We improved the surface protection by depositing previously a Pd–Au coating (Fig. 5b). The 002LF images have been carried out on a virgin nuclear graphite section prepared by FIB, and showed perfectly stacked graphene layers in all over the top surface.

The sidewall damage is unavoidable in the FIB preparation of the TEM specimen. This damage effects can be reduced significantly by using low acceleration voltages for the ion beam, reducing the thickness of the amorphous layer [55]. With all these precautions, the alteration of the TEM graphite observation could be successfully avoided.

4. Conclusion

We have shown that it is possible to prepare high-quality TEM ultra-thin sections of ion-implanted graphite for high resolution imaging, using the FIB technique. A pertinent coupling of Raman microspectrometry and TEM (11DF and 002LF modes) highlights the structural damage in graphite induced by ion implantation. Raman results revealed a significant increase of I_{D1}/I_G ratio after chlorine implantation predicting a strong disorder increase near the surface. The development of this disorder is confirmed by TEM and directly imaged by using thin sections prepared by FIB. Such sections allow the imaging of a gradient of structural changes from virgin graphite up to a highly disordered carbon near the surface. 11DF images show a strong decrease of the crystallite size. For a fluence of $5 \cdot 10^{13}$ ions/cm^2, a true amorphous carbon is not reached, since nanometer-length fringes remains visible as shown by 002LF.

Acknowledgements

The authors thank D. Troadec from IEMN (Lille, France) who granted access to the FEI Model 200 FIB system. We also thank P. Beaunier, S. Casale and D. Brouri for access to TEM facilities

UPMC (Paris, France). They are also very indebted to L. Raimbault (Ecole des Mines de Paris, Fontainebleau, France) for his help with SIMS analyses, P. Sainsot from INSA (Lyon, France) for the analyses using optical interferometry, and B. Velde from ENS (Paris, France) for the revision of the English writing. This work was supported by the European project CARBOWASTE (Treatment and disposal of irradiated graphite and other carbonaceous wastes) FP7-211333 and ANDRA (Agence Nationale pour la gestion des déchets radioactifs).

REFERENCES

[1] Lee EH. Ion-Beam Modification of Polymeric Materials: Fundamental Principles and Applications. Nucl Instrum Meth Phys Res B 1999;151:29–41.
[2] Calcagno L, Foti G. Ion irradiation of polymers. Nucl Instrum Meth Phys Res B 1991;59–60:1153–8.
[3] Klaumunzer Q, Zhu Q, Schnabel W, Schumacher G. Ion-beam-induced crosslinking of polystyrene – still an unsolved puzzle. Nucl Instrum Meth B 1996;116:154–8.
[4] Du G, Prigodin VN, Burns A, Joo J, Wang CS, Epstein AJ. Unusual semimetallic behavior of carbonized ion-implanted polymers. Phys Rev B 1998;58:4485–95.
[5] Du G, Burns A, Prigodin VN, Wang CS, Joo J, Epstein AJ. Anomalous Anderson transition in carbonized ion-implanted polymer *p*-phenylenebenzobisoxazole. Phys Rev B 2000;61:10142–8.
[6] Aleshin AN, Mironkov NB, Suvorov AV, Conklin JA, Su TM, Kaner RB. Transport properties of ion-implanted and chemically doped polyaniline films. Phys Rev B 1996;54:11638–43.
[7] Perez FJ, Hierro MP, Gomez C, Martinez L, Duday D. Silicon ion implantation on austenitic and ferritic stainless steels against localized aqueous corrosion. Surf Coat Technol 2000;133–134:344–50.
[8] Dearnaley G. Techniques and equipment for non-semiconductor applications of ion implantation. Nucl Instrum Meth 1981;189:117–32.
[9] Srinivasan V, Meier GH, McCormick AW, Rai AK. Ion implantation and thermal oxidation. Nucl Instrum Meth Phys Res B 1986;16:293–300.
[10] Niwase K, Tanabe T. Modification of graphite structure by D^+ and He^+ bombardment – II. J Nucl Mater 1991;179–181:218–22.
[11] Crowder BL. Ion Implantation in Semiconductors and Other Materials. NY: Plenum Press; 1972.
[12] Was GS. Fundamentals of radiation materials science: metals and alloys. Springer; 2007.
[13] Chi SH, Kim GC. Comparison of 3 MeV C^+ ion-irradiation effects between the nuclear graphites made of pitch and petroleum cokes. J Nucl Mater. 2008;381:98–105.
[14] Lespade P, Marchand A, Couzi M, Cruege F. Caractérisation de matériaux carbones par microspectrometrie Raman. Carbon 1984;22:375–85.
[15] Watanabe H, Iwaki M. Effects of ion implantation on structures of ion-plated carbon films. Surf Coat Technol 2009;203:2403–5.
[16] Chen C, Weng KW, Chao CH, Lien SY, Han S, Chen TL, et al. Effects of CPII implantation on the characteristics of diamond-like carbon films. Appl Surf Sci 2009;255:7216–20.
[17] Baba Y, Nagata K, Takahashi S, Nakamura N, Yoshiyasu N, Sakurai M, et al. Surface modification on highly oriented pyrolytic graphite by slow highly charged ions. Surf Sci 2005;599:248–54.
[18] Liu J, Yao HJ, Sun YM, Duan JL, Hou MD, Hou D, et al. Temperature annealing of tracks induced by ion irradiation of graphite. Nucl Instrum Meth Phys Res B 2006;245:126–9.
[19] Rouzaud JN, Oberlin A, Beny-Bassez C. Carbon films: structure and microtexture (optical and electron microscopy, Raman spectroscopy). Thin Solid Films 1983;105:75–96.
[20] Rouzaud JN, Oberlin A. Structure, microstructure and optical properties of anthracene and saccharose-based carbons. Carbon 1989;27:517–29.
[21] Beyssac O, Rouzaud JN, Goffé B, Brunet F, Chopin C. Graphitization in a high-pressure, low-temperature metamorphic gradient: a Raman microspectroscopy and HRTEM study. Contrib Mineral Petrol 2002;143:19–31.
[22] Quirico E, Rouzaud JN, Bonal L, Montagnac G. Maturation grade of coals as revealed by Raman spectroscopy: progress and problems. Spectrochim Acta 2005;61:2368–77.
[23] Jantou V, Turmaine M, West GD, Horton MA, McComb DW. Focused ion beam milling and ultramicrotomy of mineralised ivory dentine for analytical transmission electron microscopy. Micron 2009;40:495–501.
[24] E.P. Vicenzi, P.J. Heaney Examining Martian alteration products using in-situ TEM sectioning: a novel application of the focused ion beam (FIB) for the study of extraterrestrial material, 30th Annual Lunar and Planetary Science Conference, March 15–29; 1999, Houston, Abstract no. 2005.
[25] Wirth R. Focused Ion Beam (FIB): a novel technology for advanced application of micro-and nanoanalysis in geosciences and applied mineralogy. Eur J Mineral 2004;16:863–76.
[26] Heaney PJ, Vicenzi EP, Giannuzzi LA, Livi KJT. Focused ion beam milling: a method of site-specific sample extraction for microanalysis of Earth and planetary materials. Am Mineral 2001;86:1094–9.
[27] Lee MR, Bland PA, Graham G. Preparation of TEM samples by focused ion beam (FIB) techniques: applications to the study of clays and phyllosilicates in meteorites. Mineral Mag 2003;67:581–92.
[28] Stöckhert B. Focused ion beam technique and transmission electron microscope studies of microdiamonds from the Saxonian Erzgebirge, Germany. Earth Planet Sci Lett 2003;210:399–410.
[29] Obst M, Gasser P, Mavrocordatos D, Dittrich M. TEM-specimen preparation of cell/mineral interfaces by focused ion beam milling. Am Mineral 2005;90:1270–7.
[30] Smith CL, Lee MR, MacKenzie M. New opportunities for nanomineralogy using FIB, STEM/EDX and TEM. Microscopy and Analysis 2006;111:17–20.
[31] Saka H. Transmission electron microscopy observation of thin foil specimens prepared by means of a focused ion beam. J Vac Sci Technol B 1998;16:2522–7.
[32] Overwijk MHF, Van Den Heuvel FC, Bulle-Lieuwma CWT. Novel scheme for the preparation of transmission electron microscopy specimens with a focused ion beam. J Vac Sci Technol B 1993;11:2021–4.
[33] Levi RS, Fox TR, Lam K. Ion channeling effects in scanning ion microscopy with a 60 keV Ga^+ probe. Nucl Instrum Methods Phys B 1983;205:299.
[34] Evason AF, Cleaver JRA, Heard PJ, Ahmed H. Registration mark detection for scanning ion beam lithography. Electron Lett 1985;21:629.
[35] Casey JD, Doyle AF, Lee RG, Stewart DK, Zimmermann H. Gas-assisted etching with focused ion beam technology. Microelectron Eng 1994;24:43.
[36] Shaver DC, Ward BW. Integrated circuit diagnosis using focused ion beams. J Vac Sci Technol B 1986;4:185.
[37] Harriot LR, Wagner A, Fritz F. Integrated circuit repair using focused ion beam milling. J Vac Sci Technol B 1986;4:181.

[38] Toida H, Terashima K, Kobayashi T, Osada M, Watanabe K, Iwaki M. Densification of glassy carbon by fluorine ion implantation. Nucl Instrum Meth Phys Res B 2001;175–177:532–6.
[39] Benninghoven A, Rudenauer FG, Werner HW. Secondary ion mass spectrometry. New-York: Wiley; 1987.
[40] Pipon Y, Toulhoat N, Moncoffre N, Jaffrézic H, Gavarini S, Martin P, et al. Thermal diffusion of chlorine in uranium dioxide. Radiochim Acta 2006;94:705–11.
[41] Wirth R. Focused Ion Beam (FIB) combined with SEM and TEM: Advanced analytical tools for studies of chemical composition, microstructure and crystal structure in geomaterials on a nanometre scale. Chem Geol 2009;261:217–29.
[42] Everall NJ, Lumsdon J, Christopher DJ. The effect of laser-induced heating upon the vibrational Raman spectra of graphites and carbon fibres. Carbon 1991;29:133–7.
[43] Kagi H, Tsuchida I, Wakatsuki M, Takahashi K, Kamimura N, Iuchi K, et al. Proper understanding of down-shifted Raman spectra of natural graphite: direct estimation of laser-induced rise in sample temperature. Geochim Cosmochim Acta 1994;58:3527–30.
[44] Oberlin A. Chemistry and physics of carbon. In: Thrower PA, editor. New York: Marcel Dekker; 1989. p. 1–143.
[45] Petitgrand S, Yahiaoui R, Danaie K, Bosseboeuf A, Gilles JP. 3D measurement of micromechanical devices vibration mode shapes with a stroboscopic interferometric microscope. Opt Lasers Eng 2001;36:77–101.
[46] Vaudey CE, Toulhoat N, Moncoffre N, Bérerd N, Raimbault L, Sainsot P, et al. Thermal behaviour of chlorine in nuclear graphite at a microscopic scale. J Nucl Mater. 2009;395:62–8.
[47] Ziegler JF, Biersaack JP, Littmark U. In: The stopping and range of ions in solids. New York: Pergamon Press; 1985.
[48] Nemanich RJ, Solin SA. First and second order Raman scattering from finite size crystals of graphite. Phys Rev B 1979;20:392–401.
[49] Tuinstra F, Koenig JL. Raman spectrum of graphite. J Chem Phys 1970;53:1126–30.
[50] Dresselhaus MS, Dresselhaus G. Topics in applied physics. Berlin: Springer-Verlag; 1982. 3–57.
[51] Beny-Bassez C, Rouzaud JN. Scanning electron microscopy, vol. I. IL 60666 USA: SEM Inc., AMF O'Hare (Chicago); 1985. pp. 119.
[52] Sadezky A, Muckenhuber H, Grothe H, Niessner R, Pöschl U. Raman microspectroscopy of soot and related carbonaceous materials: spectral analysis and structural information. Carbon 2005;43:1731–42.
[53] Ke X, Bals S, Negreira AR, Hantschel T, Bender H, Van Tendeloo G. TEM sample preparation by FIB for carbon nanotube interconnects. Ultramicroscopy 2009;109:1353–9.
[54] Drobne D, Milani M, Leser V, Tatti F. Surface damage induced by FIB milling and imaging of biological samples is controllable. Microsc Res Tech 2007;70:895–903.
[55] Wang Z, Kato T, Hirayama T, Kato N, Sasaki K, Saka H. Surface damage induced by focused ion beam milling in a Si/Si p–n junction cross-sectional specimen. Appl Surf Sci 2005;241:80–6.